Investigations of Unsteady Transonic and Supersonic Wake Flow of Generic Space Launcher Configurations Using Zonal RANS/LES and Dynamic Mode Decomposition

V. Statnikov, T. Sayadi, M. Meinke, P. Schmid, and W. Schröder

Abstract Dynamic mode decomposition (DMD) is applied to time-resolved results of zonal RANS/LES computations of three different axisymmetric generic space launcher configurations having freestream Mach numbers of 0.7 and 6.0. Two different after-body geometries consisting of an attached sting support mimicking an endless nozzle extension and an attached cylindrical after-expanding nozzle are considered. The distinguishing feature of the investigated configurations is the presence of a separation bubble in the wake region. The dynamics of the bubble and the dominant frequencies are analyzed using DMD. The results are then compared to the findings of spectral analysis and temporal filtering techniques. The transonic case displays distinct peaks in the Fourier transform spectra. We illustrate a close agreement between the frequencies of the DMD modes and the aforementioned peaks. From the shape of the DMD modes, it is deduced that most of the peaks are related to the dynamics of the separation bubble and the corresponding shear layer. The same geometry with higher Mach number shows the existence of two distinct DMD modes of axisymmetric and helical nature, respectively. The presence of the helical mode is illustrated through composite DMD of the cylindrical velocity components. Finally, when considering the free-flight configuration we were able to identify DMD modes with frequency $Sr_D \approx 1$ which results in the flapping motion of the shear layer and a mode of a lower frequency which causes the breathing of the recirculation bubble.

1 Motivation and Objectives

Although in most cases the base geometry of a space launcher is quite simple and can be generically modeled by two coaxial cylinders mimicking the main body and the attached nozzle extension, the wake flow field is determined by different intricate

V. Statnikov (✉) • T. Sayadi • M. Meinke • P. Schmid • W. Schröder
Institute of Aerodynamics, RWTH Aachen University,
Wüllnerstr. 5a, 52062 Aachen, Germany
e-mail: v.statnikov@aia.rwth-aachen.de

unsteady phenomena such as flow separation at the base shoulder, reattachment of the shear layer at the outer nozzle wall, interaction with the jet plume, etc. It is generally known that the base drag of axial cylindrical bodies, which is caused by the low pressure at the recirculation area at the base, constitutes up to 35 % of the overall drag as shown by Rollstin [1]. Moreover, the unsteady dynamics of the separation bubble, the reattaching shear layer and their interaction lead to significant wall pressure oscillations and, consequently, dynamic loads that may excite critical structural modes which is broadly known as a buffeting phenomenon. At supersonic speeds, the wake is dominated by shock and expansion waves, drastically changing the dynamic wake flow behavior. Moreover, at higher altitudes the nozzle usually operates at under-expanded mode with a strongly after-expanding jet plume. The resulting displacement effect on the base flow generated by a wide jet plume leads to an increase of the base pressure level and, consequently, to a reduction of the base drag. On the other hand, the periodic and stochastic base pressure oscillations become stronger and might excite vibrations of critical amplitude. In addition to the aero-elastic aspects, convection of the hot gases from the jet upstream to the base area driven by the recirculation zones can lead to confined hot spots and thermal loads of the structure.

For these reasons, an accurate prediction of the wake dynamics and an understanding of its dynamics and controllability is of vital importance for the development of efficient and safe space transportation systems. Different aspects of the wake flow have been investigated in the past experimentally and numericallly. Mathur and Dutton [2] addressed base drag reduction effects of base bleeding at supersonic conditions with $Ma_\infty = 2.46$. Janssen and Dutton [3] experimentally investigated the temporal behavior of the supersonic base flow and detected dominant frequencies around $Sr_D = 0.1$ of the wall pressure fluctuations referred to inner motion of the large structures inside the separation region. The interaction of the supersonic base flow at $Ma_\infty = 2$ and 3 with an after-expanding nozzle jet was studied by Bannink et al. [4] and by Oudheusden et al. [5] who also observed several dominant lower frequencies tracked back to dynamics of the separation bubble while higher frequencies were attributed to shed turbulent structures. In the transonic regime, the buffeting phenomenon was experimentally addressed by Deprés [6] who investigated dynamics of the wake of the main stage of Ariane 5 in ONERA's S3Ch wind tunnel and detected dominant peaks in the wall pressure signal at $Sr_D = 0.2$ and 0.6. The performed two-point correlation measurements showed that the flow is dominated by a highly coherent antisymmetric mode at the vortex shedding frequency. Meliga and Reijasse [7] extended the experimental investigations on a set-up of Ariane 5 with solid boosters and detected a shift of the dominant frequency of the wall pressure fluctuations to $Sr_D = 0.34$ assumed to be caused by an axi-symmetric mode. The wake flow has also been studied numerically using turbulence models that range from various Reynolds-averaged Navier-Stokes (RANS) models [8, 9] via detached-eddy simulations (DES) [10, 11] and large-eddy simulations (LES) [12] to direct numerical simulations (DNS) [13–15]. RANS models were found to be suitable only for prediction of the attached flow and fail to provide accurate results concerning the low pressure recirculation area behind

the base. DNS is still restricted to low Reynolds numbers and a small integration domain. In contrast, LES (Meliga et al. [16]) and particularly hybrid approaches like DES (Deck and Thorigny [17]) and zonal RANS/LES (Statnikov et al. [18]) allow time-resolved computation of the dynamic wake flow field at practically relevant Reynolds-numbers and were found to be a good compromise between costs and accuracy for computation of the wake flow of space launchers.

The objective of this work is to study the numerically computed turbulent wakes of generic space launcher configurations in order to better understand the base-flow dynamics and its controllability. As shown by Statnikov et al. [18–20] for both transonic and supersonic cases, numerical results such as computed flow field topology, time-averages and fluctuations of base pressure signals as well as its spectra satisfactorily agree with the experimental data from literature and experimental investigations conducted within TRR 40 [21–23]. Using classical spectral analysis and correlation methods, several distinct frequencies were identified indicating a periodic behavior of the base-flow dynamics, e.g., $Sr_D = 0.1$ (shear layer flapping), $Sr_D = 0.2$ (von Kármán vortex shedding) as well as a number of dominant peaks at lower ($Sr_D \approx 0.05$) and considerably higher frequencies ($Sr_D \approx 0.7$ and $Sr_D \approx 1$) with not fully understood origins.

Since the wake dynamics is to a great extent dominated by a superposition of different periodic and stochastic flow phenomena, the detection of responsible coherent flow structures by using classical statistical data analysis is still a difficult task. In this respect, a combined application of Dynamic Mode Decomposition (DMD), classical statistical analysis and temporal filtering methods to the computed flow fields is a promising approach for a precise identification of significant coherent flow structures responsible for the observed unsteady behavior. As demonstrated in the paper at hand, this method allows a straightforward detection of the underlying coherent flow motion, yields a better understanding of the base-flow dynamics, and may aid in the development of efficient active and passive base-flow control mechanisms. Furthermore, DMD is applicable to any choice of flow quantity as well as to a combination of different quantities (composite DMD). Thus, composite DMD is applied to a variety of flow variables in an attempt to establish a correlation and interaction pattern between different flow quantities, e.g., pressure, velocity, and vorticity. Each DMD mode represents an optimal phase-averaged structure with a unique frequency in contrast to POD, where each mode is a multi-frequency signal. This makes DMD suitable for analyzing broadband spectra with pronounced peaks, in which the coherent flow patterns can be separated from the stochastic background fluctuations as is the case in turbulent rocket wakes.
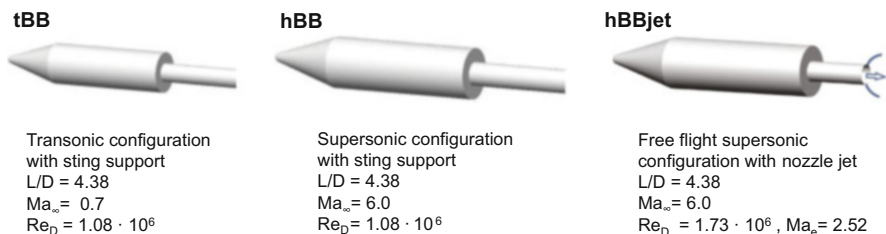
This paper is organized as follows. In Sect. 2 the three different computational setups are presented along with the respective flow parameters. Furthermore, a brief description of the computational method is provided. Dynamic mode decomposition is briefly described in Sect. 3. The results of the current approach for the three different flow geometries are presented and discussed in Sect. 4. Finally, a summary and conclusions of the current study are given in Sect. 5.

2 Computational Setups

Two different supported wind tunnel models and one free-flight configuration generically approaching an Ariane V-like launcher are considered, Fig. 1. The wind tunnel models feature an attached sting support mimicking an endless nozzle extension, while the free-flight configuration possesses an attached cylindrical after-expanding truncated ideal contour (TIC) nozzle. The same as for the main stage of Ariane V launcher, nozzle-main body ratios of $d_{nozzle}/D_{main\,body} \approx 0.4$ and $l_{nozzle}/D_{main\,body} \approx 1.2$ are used.

Two assumed trajectory points of an Ariane V-like space launcher are defined at transonic ($Ma_\infty = 0.7$, $Re_D = 1.08 \cdot 10^6$) and supersonic ($Ma_\infty = 6.0$, $Re_D = 1.73 \cdot 10^6$) conditions that follow the corresponding wind tunnel tests carried out in the framework of the TRR 40 project.

Time-resolved numerical computations of the flow field around the generic rocket configurations are performed using a zonal RANS/LES approach [24–26]. In this approach the computational domain is split into two zones, see Fig. 2. In the zone with an attached flow, e.g., the main body and the inner nozzle flow, the turbulent flow field is predicted by solving Reynolds-averaged Navier-Stokes (RANS) equations. In the wake region a large eddy simulation (LES) is performed. Using such a hybrid approach allows an efficient time-resolved computation of the dynamic wake flow field via LES at a fraction of the costs of a pure LES. The computations are done on a structured vertex-centered multi-block grid using an in-house zonal RANS/LES finite-volume flow solver. The Navier-Stokes equations of three-dimensional unsteady compressible flow are discretized in conservative form by a mixed centered upwind AUSM (advective upstream splitting method) scheme [27] of second-order accuracy for the Euler terms and by a second-order accurate, centered approximation for the viscous terms with low numerical dissipation. The temporal integration is performed by an explicit 5-stage Runge-Kutta method with second-order accuracy. The LES formulation is based on the monotone integrated LES (MILES) approach [28] modeling the impact of the sub-grid scales by numerical dissipation. A detailed description of the fundamental LES solver is given by Meinke et al. [29] and its convincing solution quality for fully turbulent sub- and supersonic flows is e.g. discussed in Alkishriwi et al. [30]

tBB

Transonic configuration
with sting support
L/D = 4.38
Ma_∞ = 0.7
Re_D = 1.08 · 10⁶

hBB

Supersonic configuration
with sting support
L/D = 4.38
Ma_∞ = 6.0
Re_D = 1.08 · 10⁶

hBBjet

Free flight supersonic
configuration with nozzle jet
L/D = 4.38
Ma_∞ = 6.0
Re_D = 1.73 · 10⁶ , Ma_e = 2.52

Fig. 1 Investigated generic space launcher configurations
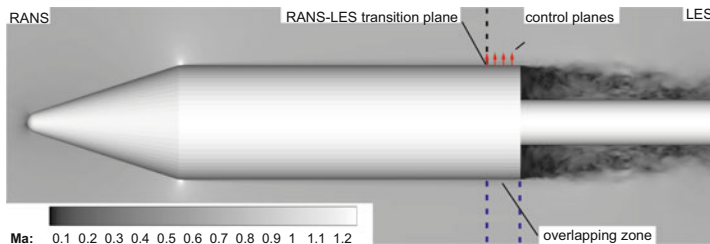
Fig. 2 Flow field decomposition into RANS and LES zones

and El-Askary et al. [31]. The RANS equations are descretized using the same overall discretization scheme. A one-equation turbulence model of Spalart and Almaras [32] is employed to close the time-averaged equations.

The transition from the RANS to the LES zone is performed by applying Refomulated Synthetic Turbulence Generation (RSTG) methods developed by Roidl et al. [24–26] that allow a reconstruction of the time-resolved turbulent fluctuations from the time-averaged upstream RANS solution. The RSTG methods are based on the synthetic eddy method (SEM) of Jarrin et al. [33] and Pamiès et al. [34] and describe turbulence as a superposition of coherent structures. These structures are generated over the LES inlet plane by superimposing virtual eddy cores which are defined in a virtual volume V_{virt} around the inlet plane that has the streamwise, wall-normal, and spanwise dimensions of the turbulent length scale l_x, the boundary-layer thickness at the inlet δ_0, and the width of the computational domain L_z. The turbulent length scales that describe the spatial properties of the synthetic structure depend on the distance from the wall and are derived from the turbulent viscosity μ_t of the upstream RANS solution and scaled with the Reynolds number and the associated convection velocity. As a result, the final velocity signal is composed of an averaged velocity component $\overline{u_i}$ which is provided from the upstream RANS solution and the normalized stochastic fluctuations u_i' which are subjected to a Cholesky decomposition to assign values of the Reynolds-stress tensor corresponding to the turbulent eddy viscosity.

To minimize the transition zone between the RANS and LES domains, controlled body forces f_i can be added to the wall-normal momentum equation at a number of control planes at different streamwise positions to enforce a match of the turbulent flow properties of the LES with the given RANS values as shown in Fig. 2. The amplitude of the force term is defined by a proportional integral controller, which controls the deviation between the target and the current profile of the reconstructed Reynolds shear stresses. A detailed description of the methods including the shape functions and length scale distributions is given in [24, 25].

3 Dynamic Mode Decomposition (DMD)

DMD is performed using the algorithm presented in [35], with a preprocessing step based on a singular value decomposition. This implementation allows for rank-deficient snapshot sequences, and it avoids ill-conditioned companion matrices [36]. In its simplest form, DMD provides the following representation of a flow field U,

$$U(x, y, z, t) = \sum_{n=1}^{N} a_n \exp(\lambda_n t) \phi_n(x, y, z), \tag{1}$$

where x, y, and z are spatial coordinates and t is time. In Eq. (1), ϕ_n's are the DMD modes, a_n's are the amplitudes and λ_n's are the frequencies of the respective modes. ϕ_n, a_n, and λ_n are complex-valued quantities. The eigenvalues of the modes can be deduced from the frequencies following the relation, $\lambda_n = log(\mu_n)/\Delta t$, where μ_n are the eigenvalues of the coupled inter-snapshot mapping and Δt is the time step between two consecutive snapshots. In DMD, the modes and frequencies are determined without the need for specifying an inner product or a norm. Compared to POD, this gives DMD the advantage of being applicable to any choice of flow quantities or spatial domains.

Once the modes and frequencies of the system are computed, we recover the complex amplitudes through a reconstruction of the original data. To solve for the magnitudes of each mode, a_n, we apply a pseudo-inverse to find the bi-orthogonal basis, ψ, of dynamic modes, ϕ such that

$$< \psi_i . \phi_j >= \int \psi_i^* \phi_j dV = \begin{cases} 0, i \neq j \\ 1, i = j. \end{cases} \tag{2}$$

While this could be done over all snapshots, in this report we choose to apply the pseudo-inverse to the first snapshot only, and then use the remaining snapshots to evaluate the closeness of fit for later times. If the dynamic modes are normalized, $|\tilde{a}_n|$ gives the relative magnitude of the nth mode. This algorithm has been applied to the direct numerical simulation (DNS) data of H-type transition on a flat-plate boundary layer [37].

4 Results

The results are discussed in three sections. In Sect. 4.1 the post-processing methodology is applied to the unsteady streamwise velocity field in the near wake of the supersonic free-flight configuration with after-expanding jet. Particular attention is paid to an interpretation of the extracted DMD modes required for understanding the results presented in the following sections. In the next section the transonic wake is

considered and the existent peaks in the Fourier spectra of the pressure signal in the vicinity of the separation bubble are interpreted using DMD. In addition, the concept of composite DMD is introduced and applied to the pressure and velocity signals. Finally, in Sect. 4.3, composite DMD is performed on the cylindrical velocity components of the hypersonic wake of the same geometry as the transonic setup.

4.1 DMD Analysis of the Free-Flight Configuration

To introduce the applied post-processing methodology, the wake dynamics of the free-flight configuration is analyzed. At the base shoulder, the supersonic boundary layer separates and undergoes an expansion leading to formation of a low-pressure region and subsonic recirculation zone associated with radial deflection of the shear layer towards the axis of symmetry. Farther downstream, a strongly after-expanding jet plume emanates from the nozzle leading to a displacement effect on the base flow. As a result, the main body shear layer is reflected away from the nozzle wall and no reattachment occurs. Thus, a confined subsonic cavity region is formed between the base and jet plume in the axial direction as well between the nozzle wall and shear layer in the radial direction. The resulting wake flow topology is presented in Fig. 3 showing the time-averaged axial velocity, Mach-number and streamline distribution.

The flow behind the base shoulder and just in front of the nozzle, which includes the separation bubble and the cavity, is investigated using DMD. Figure 4a shows
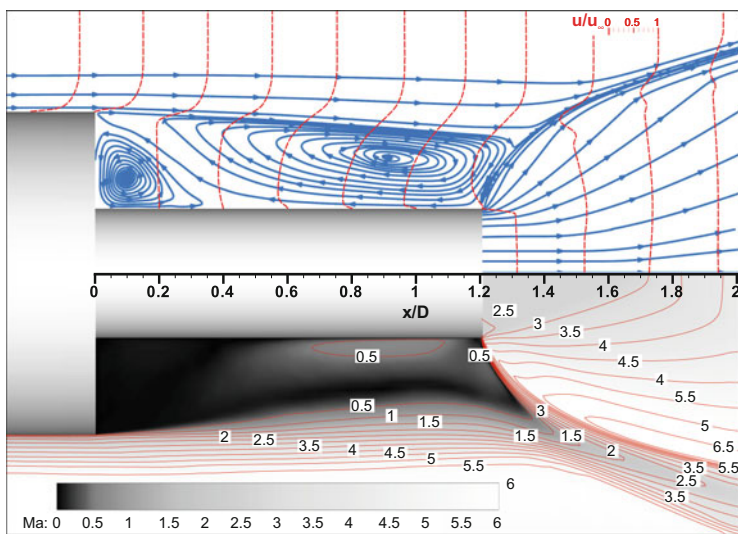
Fig. 3 Time-averaged axial velocity, Mach-number and streamlines distribution in the wake of the free-flight configuration
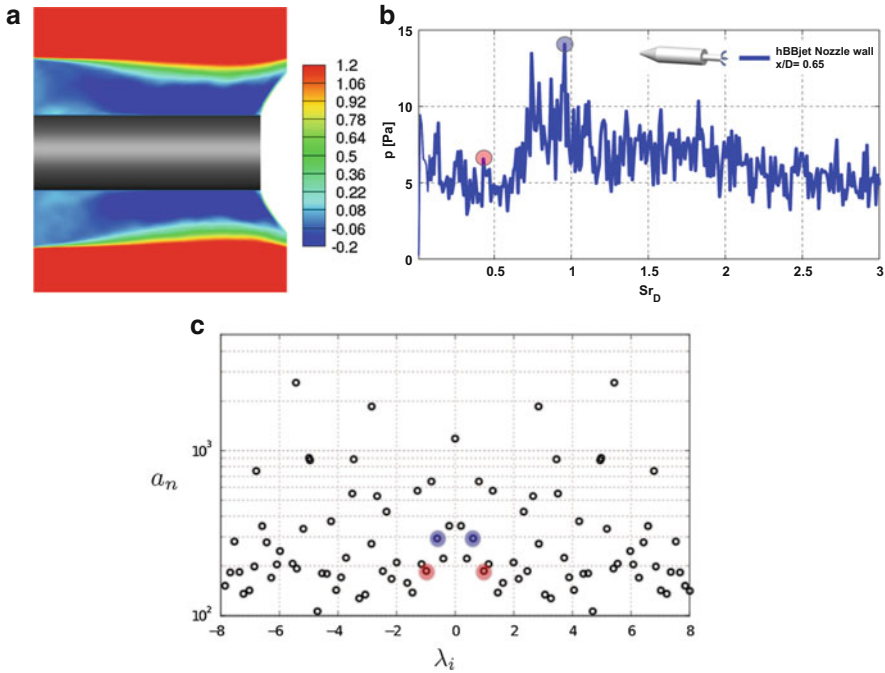
Fig. 4 DMD of the *u*-velocity field of the transonic configurations. (**a**) Mean velocity flow field in the $x - y$ slice of the thee-dimensional flowfield. (**b**) DFT of the pressure fluctuations. •, $Sr_D = 0.4$; •, $Sr_D = 0.98$. (**c**) DMD spectra of the u-velocity component. •, $\lambda_i = 0.4$; •, $\lambda_i = 0.98$

a cross section of the mean streamwise velocity inside this domain. The discrete Fourier transform (DFT) spectra of the pressure fluctuations at the wall can be split in two regions of low and high frequencies extending from $Sr_D = 0$ to 0.5 and $Sr_D \geq 0.5$, respectively. Inside each low-and high-frequency zones, peaks are also identified. DMD is performed on the three-dimensional data, in order to construct a global shape of the mode responsible for each frequency. In this report we concentrate on one mode in each zone of the DFT spectra shown in Fig. 4b by blue and red circles. The DMD spectra of the streamwise velocity are shown in Fig. 4c. The axis of abscissas in the plot represents the frequency of each DMD mode. From this information the modes with the same frequencies as the ones identified via the DFT spectra are chosen. These modes are shown in the plot using blue and red circles as in Fig. 4b. Figure 4c shows two frequencies in the DMD spectra corresponding to the single DFT frequency. A pair of complex conjugate modes are needed to provide the correct phase of the modes with respect to the original data. The two frequencies in the DMD spectra represent a single DMD mode.

The high-frequency DMD mode with $Sr_D = 0.98$ is shown in Fig. 5. This mode oscillates with constant frequency by construction and, to represent this oscillation,
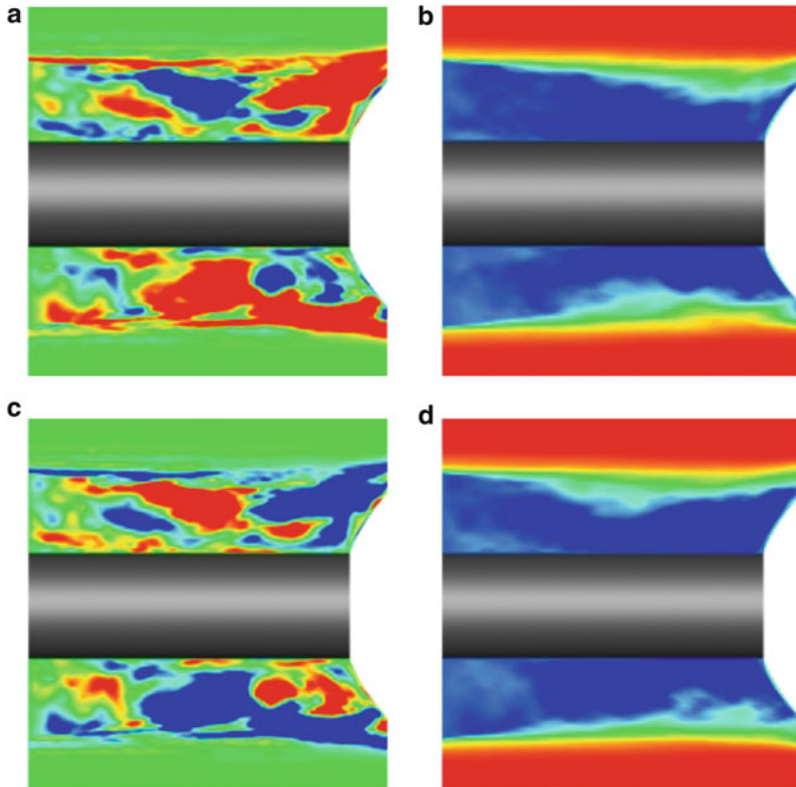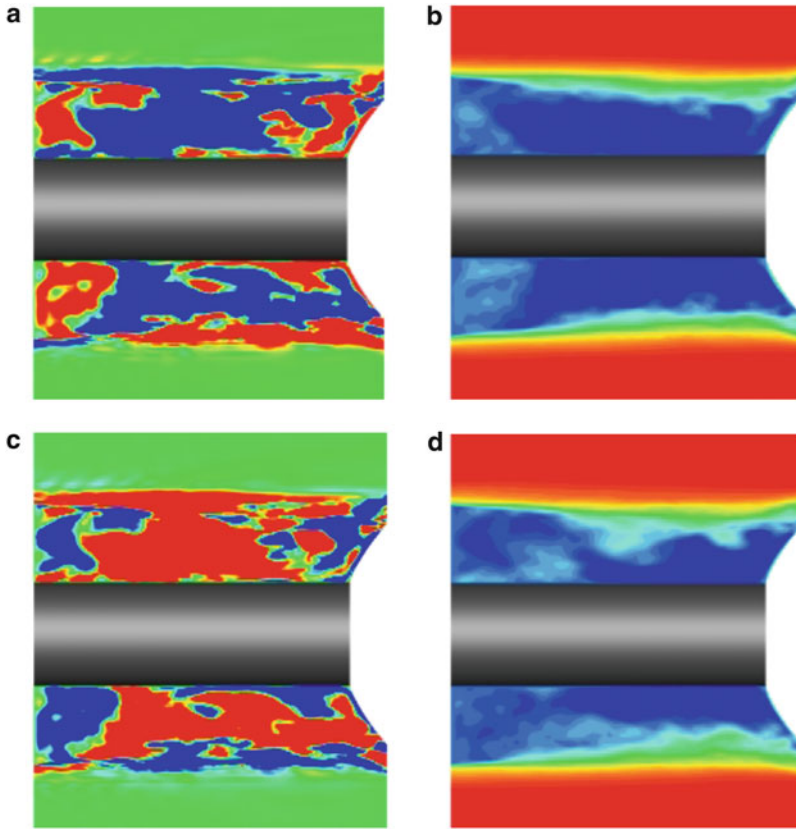
Fig. 5 DMD mode responsible for the flapping of the shear layer at frequency $\lambda_i = 0.98$. Contour levels: (*blue*), negative values; (*red*), positive values. (**a**) Mode, beginning of the cycle. (**b**) Modulation of the mean beginning of the cycle. (**c**) Mode, middle of the cycle. (**d**) Modulation of the mean middle of the cycle

the shape of the mode in the beginning and middle of each period is shown in Fig. 5a, c, respectively. The mean-flow solution shows the location of the separation bubble in a time-averaged manner. By adding the DMD mode to the time-averaged mean flow, the modulation of the mean through each mode is illustrated as shown in Fig. 5b, d for $Sr_D = 0.98$. The shape of this mode shows that the main contribution to the total mean flow is at the location of the shear layer edge. Concentrating on the upper half of the domain shown in Fig. 5a, this interaction with the mean shear is in the form of two areas of low and high velocity magnitude, which are reversed in position in the middle of the period (Fig. 5c). The lower half of the mode is 180° out of phase with the upper half. Ultimately, the combination of this mode and the mean results in the flapping of the shear layer and in this frame of reference is 180° out of phase in the upper and the lower half of the domain.

The same exercise can be performed on the mode with lower frequency. Figure 6a, c shows the mode shape in the beginning and the middle of the period. The

Fig. 6 DMD mode responsible for the bubble dynamics at frequency $\lambda_i = 0.4$. Contour levels: (*blue*), negative values; (*red*), positive values. (**a**) Mode, beginning of the cycle. (**b**) Modulation of the mean beginning of the cycle. (**c**) Mode, middle of the cycle. (**d**) Modulation of the mean middle of the cycle

modulation of the mean streamwise velocity through this mode is also demonstrated in Fig. 6b, d. In contrast to the previous results, there is little dependence on the transverse direction when the shape of the mode is considered. The mode also interacts mainly with the separation bubble itself. This is illustrated through Fig. 6b, d, which shows the increase and decrease in the size of the averaged separation bubble when the magnitude of the DMD mode is, respectively, negative or positive.

These two examples illustrate the advantage of the three-dimensional DMD, since the evolution of the flow is determined through the shape of the mode and not only the frequencies. We have also illustrated how modes of different frequencies and shape influence the dynamics of the flow by studying the interaction of each mode with the averaged solution.
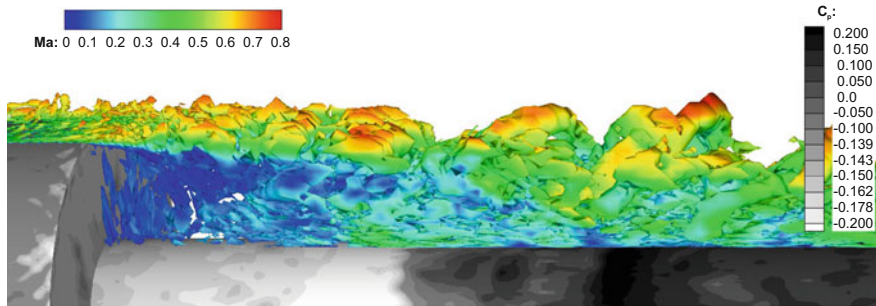
Fig. 7 Instantaneous vortex structures by means of λ_2-contours colored by Mach-number and wall-pressure coefficient distribution in the wake of the transonic configuration

4.2 Transonic Configuration

The interaction between the shedding shear-layer vortices and the main engine's nozzle reaches its maximum intensity at transonic speeds and leads to increased mechanical loads on the nozzle structure. This effect is investigated for an axisymmetric configuration at $Ma_\infty = 0.7$ shown in Fig. 1. The axisymmetric backward-facing step causes a strong separation of the incoming turbulent boundary layer leading to the formation of a low-pressure recirculation region downstream of the base. As a result, the shear layer sheds from the shoulder of the cylindrical fore-body and broadens further downstream because of turbulent mixing effects. Due to the low-pressurized region at the base, the shear layer is deflected towards the sting and reattaches forming a closed recirculation zone, Fig. 7.

To gain insight into the global wake dynamics, discrete Fourier transformation (DFT) of the pressure fluctuations are performed at several axial positions on the wall of the attached sting. Figure 8a shows the resulting spectra at three different axial positions representing regions of interest inside the recirculation bubble; close to the base ($x/D = 0.2$), at the reattachment point ($x/D = 1.2$) and downstream of the separation bubble ($x/D = 2.0$). These regions show a slight variation of the detected dominant modes and their respective amplitudes. The global averaged DFT of the pressure fluctuations on the sting is presented in Fig. 8b. Through this approach, DFT spectra of the various streamwise locations are subsequently averaged to highlight the global dominant modes. Six distinct global modes of the wall-pressure fluctuations lower than $Sr_D = 1.0$ (summarized in Table 1) are identified.

In order to extract the spatial shape of the modes associated with peaked frequencies in the globally averaged DFT spectra, DMD is performed on the streamwise field signal of the three-dimensional domain surrounding the averaged separation bubble. Figure 9a shows the eigenvalues of the DMD spectra. Since the flow is turbulent and fully non-linear we expect all eigenvalues to be on the unit circle. Figure 9a shows, however, that there are some modes with eigenvalues that
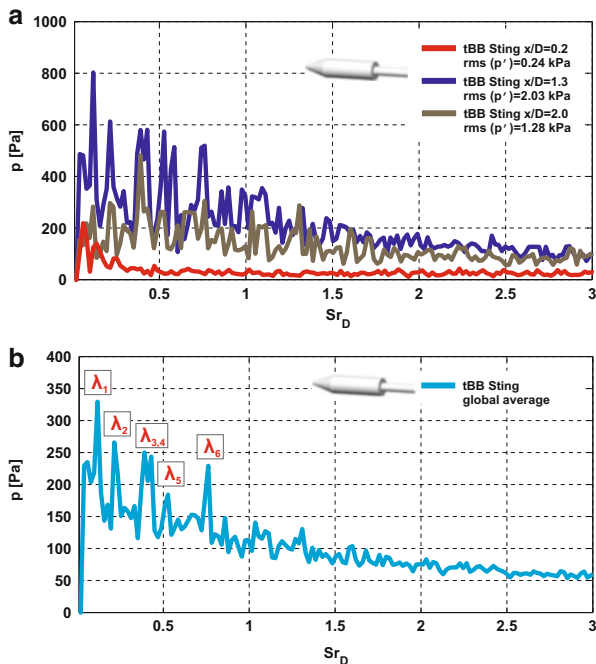
Fig. 8 DFT of the wall pressure fluctuation of the transonic configuration. (**a**) Local. (**b**) Globally averaged

lie inside the circle. These modes represent transients that have high amplitude in the beginning of the signal but are quickly damped and have little influence on the overall dynamics of the flow. As a result, in this study they are identified as transient modes and are neglected in our further analysis. Figure 9b shows the DMD spectra corresponding to the DMD eigenvalues. The transient modes can be identified by having higher magnitudes than the mean located at $\lambda_i = 0$. The amplitudes a_n's, as explained in Sect. 3, are calculated by projection on the data of the first snapshot, where these transient modes have the most contribution, which causes them to appear as artificial peaks in the DMD spectra, even though, they have a strong decay rate and are irrelevant in the global dynamics. We can therefore conclude that Fig. 8a, b each give part of the information on the significance of a single DMD mode and only by considering them together we are able to provide an accurate interpretation of the results. The low-frequency modes identified in the DFT spectra can also be extracted from DMD spectra of Fig. 9b and are represented by colored symbols. As mentioned before, each mode consists of a complex conjugate pair and can be seen in both Fig. 9a, b.

The estimated frequencies from the DMD analysis are compared to the DFT-results in Table 1. This table shows that there is good agreement between the frequencies extracted by either method. We have also analyzed the pressure signal
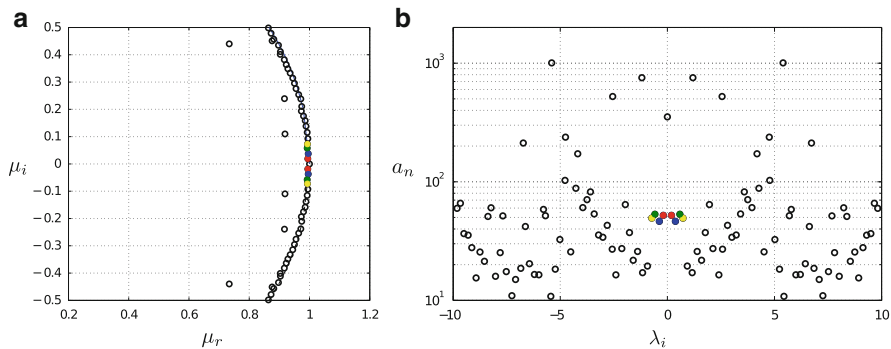
Fig. 9 DMD of the streamwise velocity of the transonic configuration. ●, λ_2; ●, λ_3; ●, λ_5; ●, λ_6. (**a**) Eigenvalues, μ. (**b**) DMD spectra

Table 1 Comparison of the frequencies extracted by using DFT and DMD

| Frequency	λ_2	λ_3	λ_4	λ_5	λ_6
DFT	0.21	0.39	0.43	0.57	0.76
DMD	0.19	0.37	0.46	0.59	0.72

at the wall, which is the signal used in the DFT analysis, and we have verified that the results remain unchanged. As DMD allows sub-domain analysis of the full data, we could also establish that mode λ_4 is relevant close to the step, since this frequency appears once the step is included in the DMD domain. Mode $\lambda_1 = 0.1$ is not detected using the DMD formalism. This mode could be a product of a non-linear interaction of two higher-frequency modes of frequencies 0.2 and 0.3 that is artificially magnified. This frequency can also be related to local dynamics close to the step. This is a plausible explanation, since Fig. 8a shows a decrease in the magnitude of this peak with an increase of the streamwise distance from the step. In DMD a larger three-dimensional domain is analyzed, which could cause the very local dynamics of the flow to remain undetected.

Figure 10 shows the instantaneous streamwise (u) and mean velocity (λ_0) contours in the domain of consideration for the DMD analysis. This figure also illustrates the shape of the modes with frequencies λ_2, λ_3, λ_5 and λ_6 which are related to the dynamics of the separation bubble. Mode λ_5 is more active close to the wall, whereas mode λ_3 has the most influence away from the wall. This can be deduced from the location of high- and low-magnitude velocities (red and blue regions) in each mode. Modes λ_2 and λ_6, however, show the most variation along the edge of the mean shear layer. Therefore, they are more relevant for the dynamics of the shear layer itself. This exercise illustrates how, with the help of DMD and extracting the three-dimensional modal shape for a single frequency from the fully turbulent data, the associated dynamics can be interpreted.

DMD is a method of data-driven spectral analysis; therefore, any type of data can be considered for evaluation. Furthermore, different flow parameters, for example vorticity, velocity, etc., can be combined as an input to this analysis (composite
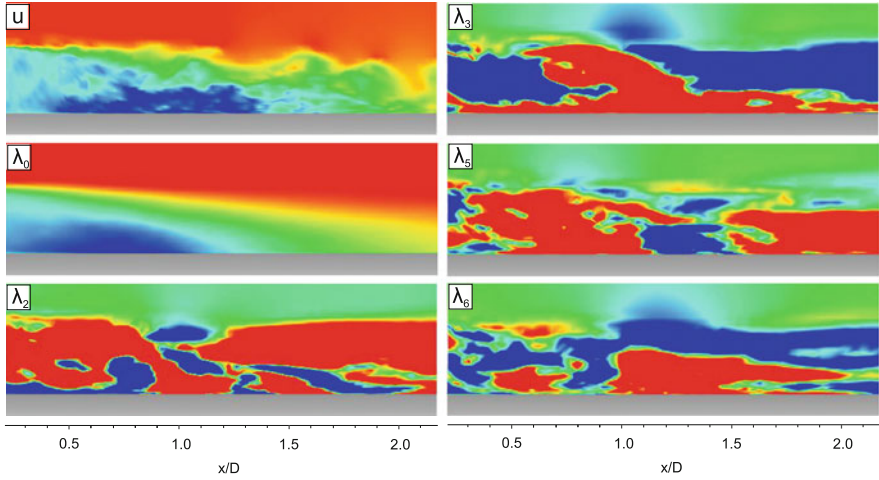
Fig. 10 Instantaneous (u) and mean velocity (λ_0) contours of the DMD domain. Mode shapes of frequencies λ_2, λ_3, λ_5 and λ_6 (*blue*: negative values; (*red*): positive values)
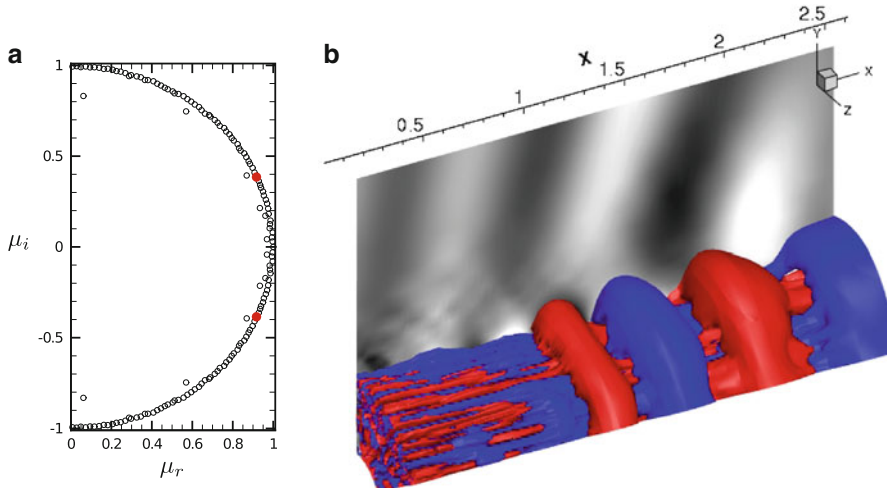

Fig. 11 Composite DMD of the pressure (*black-white* contours) and streamwise velocity (*red and blue* iso-surfaces). (**a**) Eigenvalues, μ. (*red*) $\lambda_i = 4$. (**b**) modal shape, $\lambda_i = 4$

DMD). Composite DMD allows the assessment of a coupling between various flow variables on a basis of their frequency. We have performed composite DMD on the pressure and streamwise velocity of the transonic data, and the resulting eigenvalue spectrum of this analysis is shown in Fig. 11a. For the purpose of this analysis we have considered a domain which extends further downstream than the original DMD domain. As the domain of interest is not centered on the separation bubble, other dynamics are also included. In particular, a mode of a higher frequency

$\lambda_i = 4$, shown in Fig. 11b, contains structures at the edge of the shear layer with a growing wavelength downstream. The pressure signal associated with this velocity also shows a trace in the freestream highlighted by the oscillating black and white pressure contours. This figure shows that the velocity, iso-surfaces of red and blue, are 180° out of phase with the pressure signal. In addition, by analysis of the evolution of this mode in time we have determined that the pressure in the freestream travels upstream while the velocity component is moving downstream. This is reminiscent of an acoustic wave in such circumstances, the proof of which needs further investigation.

4.3 Supersonic Configuration

In this setup the main body geometry and freestream conditions ($Ma_\infty = 6.0$) are identical to the supersonic configuration with an attached sting support presented in Sect. 4.1. Therefore, the flow along the main body up to the base shoulder is the same as for the supersonic free-flight configuration. The wake flow topologies, however, differ significantly from the free-flight case due to the use of an endless nozzle extension instead of a working TIC nozzle. As a result, no displacement effect of the jet is present and the resulting shear layer consequently is deflected towards the axis of symmetry and reattaches on the surface of the sting support. The time-averaged wake flow field is presented in Fig. 12 showing the Mach-number, static pressure ratio, streamlines, and axial velocity profiles.
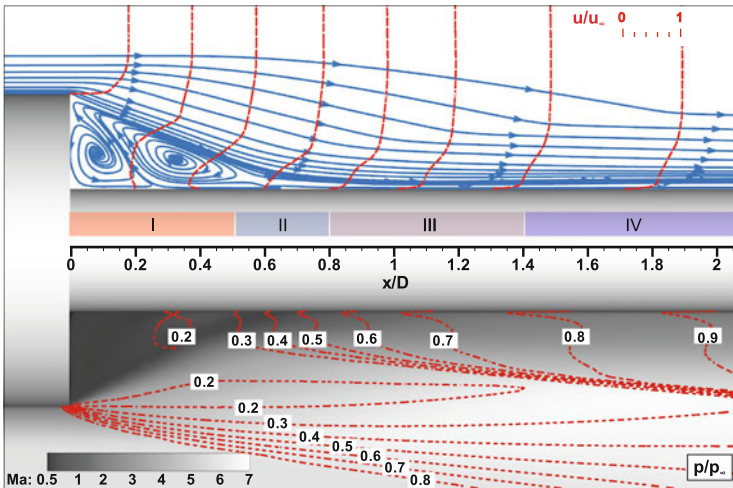
Fig. 12 Time-averaged wake flow topology of the supersonic configuration with sting. Different dynamic regions: (*i*) recirculation bubble; (*ii*) reattachment line; (*iii*) recompression waves; (*iv*) recompression shock
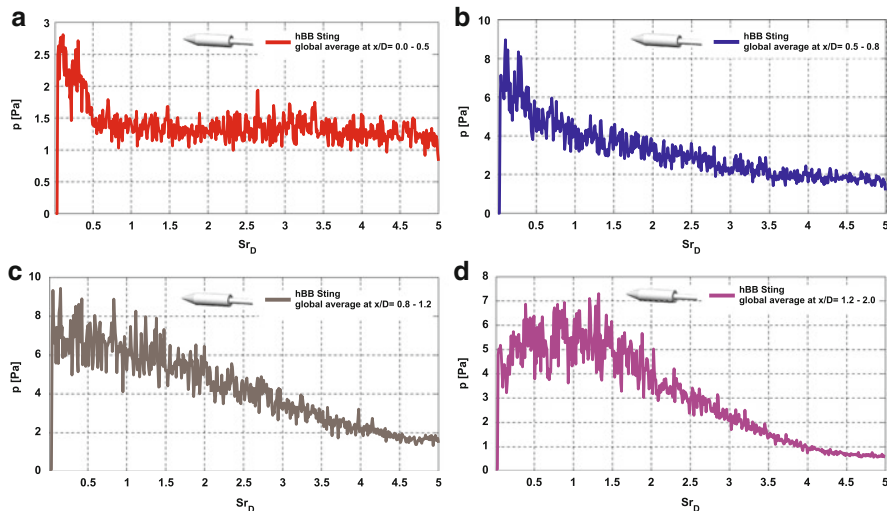
Fig. 13 DFT of the wall-pressure fluctuations for the hypersonic configuration with sting of four different dynamic regions. (**a**) Recirculation bubble (i). (**b**) Reattachment line (ii). (**c**) Recompression waves (iii). (**d**) Recompression shock (iv)

As schematically highlighted by colored rectangles in Fig. 12, the wake of the supersonic configuration can be divided into four regions; the recirculation bubble (**i**), the reattachment region (**ii**), the re-compression waves (**iii**), and the re-compression shock (**iv**). Unlike the transonic case, the dynamics and consequently the dominant frequencies at $Ma_\infty = 6.0$ differ significantly depending on each of these four regions. The spectra in the vicinity of the separation bubble show lower-frequency modes of higher amplitudes, however, the amplitude of these modes reduces as streamwise positions further downstream are considered. The spectra taken at the location of the re-compression shock show little dependance on the modal frequency. Moreover, the DFT spectra of wall-pressure fluctuations show rather dominant frequency ranges than sharp peaks of the wall-pressure fluctuations (Fig. 13). Therefore it is difficult to isolate a single frequency of interest, and for the purpose of this study a range of frequencies is classified as a frequency-domain. These frequency-domains for the region including the recirculation bubble (region (i)) are; $D_1 : 0 \le Sr_D \le 0.2$, $D_2 : 0.2 \le Sr_D \le 0.2$ and $D_3 : Sr_D > 0.5$. When applying the DMD algorithm, a frequency within the defined frequency-domain is selected to represent the dynamics within that range.

In order to remain within the scope of this report, we will concentrate on the recirculation bubble and the reattachment line; therefore, the DMD domain is restricted to regions (i) and (ii). DMD is performed on the streamwise, radial and transverse velocity components. Although DFT is performed on the wall-pressure signal, we realized that due to the presence of the shock wave inside the domain of interest the pressure has a higher value downstream than upstream. As a result the
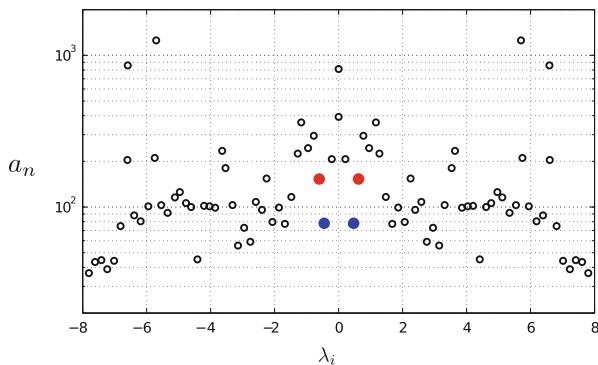
**Fig. 14** DMD spectra. •, $Sr_D = 0.4$; •, $Sr_D = 0.64$

pressure signal would be more relevant for studying the dynamics of the shockwave or the downstream pressure. Since we are interested in the separation bubble located upstream of the domain, velocity components are a better choice for the DMD analysis. In addition, composite DMD allows for a complete three-dimensional picture of the dynamics in the flow and would provide information on how each velocity component is coupled to the others within a single modal frequency. We have chosen the cylindrical rather than Cartesian velocity components in order to take advantage of the axisymmetric nature of the flow. Moreover, the presence of helical modes have been reported for these types of geometries, and the transverse velocity would allow direct assessment of the existence of such modes.

Figure 14 shows the DMD spectra of the three velocity components within the subdomain of region (i) and (ii). As mentioned previously, the modes which appear with a higher amplitude than the mean are transient modes, which decay rapidly and have only a short-term influence on the dynamics of the flow, and are therefore neglected. We have focused on the two frequency-domains of D_2 and D_3. We have chosen not to include D_1 since its dynamics is of lower frequency and more snapshots are needed to properly capture these modes correctly. The chosen DMD modes in domains D_2 and D_3 are shown in Fig. 14 by the blue and red symbols.

Figure 15a shows the shape of the DMD mode corresponding to $Sr_D = 0.4$ in D_2. For each velocity component slices in the $x - y$ and $y - z$ planes are shown. The radial velocity component of this mode is symmetric across the plane of reference of the $x - y$ slice. The $y - z$ slice of this velocity component shows that symmetry is not preserved throughout the geometry. However, this mode is not a traveling mode in the transverse direction, which is illustrated in the $y - z$ slice shown in Fig. 15b, where the modulation of the transverse mean flow due to the transverse component of the mode is plotted. This component has little effect on the mean-flow value suggesting that, although the bubble is wrinkled in the transverse direction, it represents a standing wave. The same results apply when considering the modulation of the streamwise velocity. The evolution of the mean flow through this mode shows the pinching of the separation bubble when the radial component is
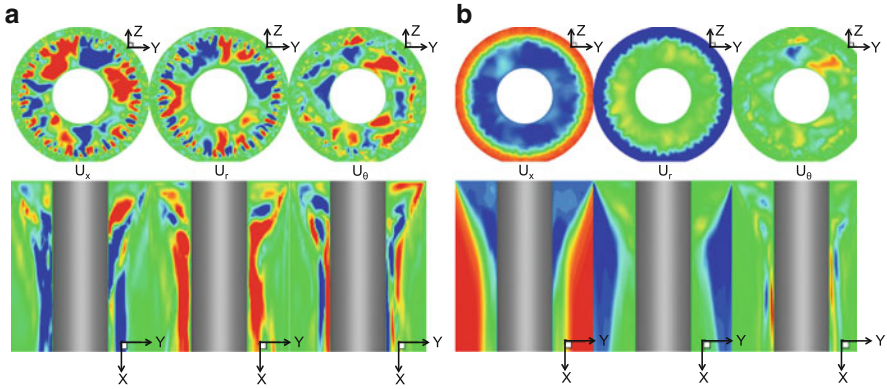
Fig. 15 DMD mode with frequency $Sr_D = 0.4$. Velocity components from *left* to *right*: U_x, streamwise velocity; U_r, radial velocity; U_θ, transverse velocity. (*Blue*), negative values; (*Red*) positive magnitude. (**a**) Velocity components of mode $\lambda_1 = 0.4$. (**b**) Velocity components the mean and mode $\lambda_1 = 0.4$
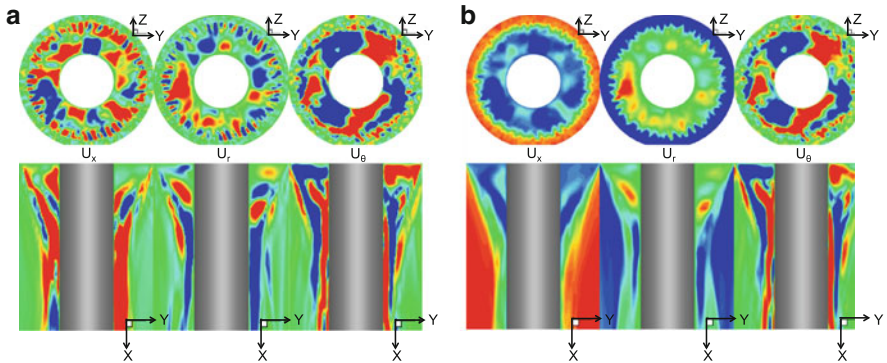
Fig. 16 DMD mode with frequency $Sr_D = 0.64$. Velocity components from *left* to *right*: U_x, streamwise velocity; U_r, radial velocity; U_θ, transverse velocity. (*Blue*), negative values; (*Red*) positive magnitude. (**a**) Velocity components of mode $\lambda_1 = 0.64$. (**b**) Velocity components the mean and mode $\lambda_1 = 0.64$

negative and the release of the bubble when the value is positive. This in turn results in the breathing of the separation bubble.

Figure 16a shows the shape of the higher-frequency DMD mode. In contrast to the lower-frequency mode this mode has a bigger signature in both the streamwise and the transverse velocity components. The mean-flow velocity is symmetric along the streamwise axis due to the presence of axi-symmetry in the mean flow. As a result, the transverse component is of negligible value, as seen in Fig. 15b. The modulated mean velocity of this higher-frequency mode, however, shows a distinct variation along the transverse direction. The evolution of this mode in time confirms

this conclusion, and the mode is shown to move along the transverse direction periodically.

Modes $\lambda_1 = 0.4$ and $\lambda_2 = 0.64$ contain two completely different dynamics of the separated flow. One mode causes the breathing of the separation bubble with a small trace in the transverse direction, while, the higher-frequency mode is of a helical nature, illustrated by the modulated mean transverse velocity component.

4.4 Computational Resources

The time-resolved zonal RANS/LES computations for this study were performed on the CRAY XE6 (Hermit) at the HLR Stuttgart. The computational grids are divided into blocks which reside on a single CPU Core. Data is exchanged using the message passing interface (MPI). The good scalability of the used house-internal zonal RANS/LES flow solver is demonstrated in Fig. 17. The computational details for the three performed simulations are given in Table 2. It is evident that the total number of the mesh points, which is the first major parameter with respect of the required computational resources, is significantly larger for the transonic case than for the hypersonic ones, even though the transonic grid spans over 60° in the circumferential direction and the hypersonic domains extend over full 360°. The main reason for this fact is that at transonic speeds the pressure waves, which propagate with the speed of sound, also travel upstream. Therefore, the boundaries of the computational domain have to be positioned at a satisfactorily large distance
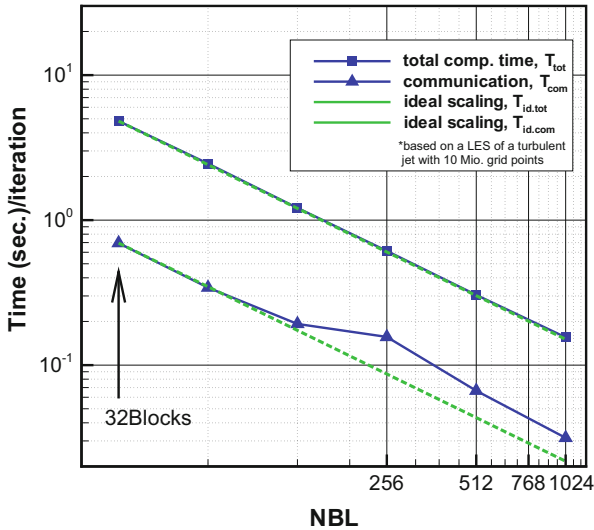

Fig. 17 Strong scaling of the used house-internal zonal RANS/LES flow solver

Table 2 Required resources for CFD computations

Configurations	Transonic w. sting	Hypersonic w. sting	Hypersonic w. jet
Total grid points	$76.1 \cdot 10^6$	$22.5 \cdot 10^6$	$35.5 \cdot 10^6$
Number of CPUs	4,096	512	1,024
Number of nodes	128	16	32
Grid points/CPU	18,557	43,946	34,667
Comp. phys. time [t_{ref}]	50	50	50
Comp. speed [t_{ref}/h]	0.5	0.1	0.13
Total. user time [h]	100	500	385
Total. core hours [CPU$\cdot$h]	0.4096 Mio.	0.2560 Mio.	1.2 Mio.
Used HDD storage [TB]	2.3	0.7	1.1

Table 3 Required resources for DMD analysis

Configurations	Transonic w. sting	Hypersonic w. sting	Hypersonic w. jet
Total grid points	$76.1 \cdot 10^6$	$22.5 \cdot 10^6$	$35.5 \cdot 10^6$
Peak RAM use [GB]	232	73	115
HDD storage/Variable [GB]	187	66	93

from the launchers body. At supersonic speeds, no flow information can travel upstream and the computational domain can be made compact covering only the bow shock region around the rocket's body. On the other hand, the hypersonic cases were found to feature a smaller time-step than their transonic counterpart, which is caused by significant compressibility effects and occurrence of strong shock waves at $Ma_\infty = 6$ limiting the numerical stability.

To assess the length of the computed physical time interval and respective computational resources required for a reliable statistical analysis of the simulation data, a reference time unit t_{ref} is used, with $1\,t_{ref}$ being the time needed by a particle moving with the freestream velocity u_∞ to cover one reference length equal to the main body diameter D of the launcher. To achieve satisfactory statistical quality, a minimum time interval of $50\,t_{ref}$ is required. Taking into account the different computational speed of each case, which depends on the total number of grid points per CPU and maximum stable time-step, we obtain the total required CPU hours summarized at the end of Table 2.

While the major requirement for the large CFD computations is the number of CPUs, the main driving parameter for the post processing of the simulation data is the virtual memory. For the performed DMD analysis, the shared node SMP of the HLR Stuttgart with 1 TB memory was used. The computational resources required for the performed DMD analysis are summarized in Table 3. The peak virtual memory use reaches up to 232 GB for the composite DMD of three velocity components. Physical storage of one post-processed variable, e.g., the axial velocity component u, requires up to 0.2 TB which linearly scales with the total number of the grid points.

5   Summary and Conclusions

The separation bubble dynamics in three different flow configurations of axisymmetric space launchers has been analyzed numerically using DMD together with a conventional discrete Fourier transform technique. The freestream Mach number has been varied from 0.7 to 6.0 consistent with the common operating points of the space launchers.

In the transonic case, DFT of the pressure fluctuations at the wall reveal distinct frequencies, which appear as peaks. We have shown that these frequencies can be extracted with close agreement using DMD. In addition, DMD provides a modal shape corresponding to each frequency. The shapes of the modes verify that the low-frequency modes are indeed related to the dynamics of the separation bubble and the reattachment line. Applying composite DMD we have been able to show the coupling between the streamwise velocity and pressure of a single high-frequency mode to be reminiscent of an acoustic wave.

The flow over the same geometry at the supersonic Mach number shows different trends in the DFT spectra. The single-frequency peaks are no longer distinguishable; instead, a region of dominant frequencies are identified, whose amplitudes decrease as we move downstream. The domain of interest encircles the separation bubble, and the DMD has been performed on this domain. Two modes within these higher and lower frequency ranges have been analyzed. The low-frequency mode is responsible for the breathing motion while the high-frequency mode produces a helical motion commonly detected in such geometries. The wave-length of this mode in the transverse direction illustrates that this mode would have been difficult to be detected without including the full geometry. Moreover, using composite DMD we have been able to establish a coupling of each velocity component with a single frequency mode.

Finally, a free-flight configuration has been considered. Although the Mach number is similar to the supersonic case, due to the presence of an after-expanding nozzle jet, the dynamics and hence the relevant frequencies change significantly. The two modes studied here display two different dynamics of the cavity flow, which develops behind the step. The DMD mode corresponding to the low-frequency range of the DFT spectra is more active close to the region of the averaged separation bubble and results in the low-frequency breathing of the bubble. In contrast, a higher-frequency mode with $Sr_D \approx 1.0$ is active in the region of the averaged shear layer edge, and in combination with the mean flow, results in the flapping motion of the shear layer.

In conclusion, although the conventional DFT offers some idea on the relevant frequencies of the flow, without a clear picture of modal shapes, the assessment of the effect of each frequency on the entire flow dynamics would be difficult. Using DMD not only provides a three-dimensional shape associated with the respective frequency, it also allows the determination of the coupling between different flow variables.

References

1. Rollstin, L.R.: Measurement of in-flight base pressure on an artillery-fired projectile. AIAA Paper **87**, 2427 (1987)
2. Mathur, T., Dutton, J.: Base-bleed experiments with a cylindrical afterbody in supersonic flow. J. Spacecr. Rockets **33**, 30–37 (1996)
3. Janssen, J., Dutton, J.: Time-series analysis of supersonic base-pressure fluctuations. AIAA J. **42**, 605–613 (2004)
4. Bannink, W., Houtman, E., Bakker, P.: Base flow / Underexpanded exhaust plume interaction in a supersonic external flow. AIAA Paper **98**, 1598 (1998)
5. Scarano, F., van Oudheusden, B., Bannink, W., Bsibsi, M.: Experimental investigation of supersonic base flow plume interaction by means of particle image velocimetry. In: 5th European Symposium on Aerothermodynamics for Space Vehicles, Cologne, pp. 601–607. Number ESA SP-563 (2004)
6. Deprés, D., Reijasse, P., Dussauge, J.: Analysis of unsteadiness in afterbody transonic flows. AIAA J. **42**, 2541 (2004)
7. Meliga, P., Reijasse, P.: Unsteady transonic flow behind an axisymmetric afterbody equipped with two boosters. AIAA Paper **4564**, (2007). doi:10.2514/6.2007-4564
8. Benay, R., Servel, P.: Two-equation k-σ turbulence model: application to a supersonic base flow. AIAA J. **39**, 407–416 (2001)
9. Papp, J., Ghia, K.: Application of the RNG turbulence model to the simulation of axisymmetric supersonic separated base flows. AIAA Paper 2001-2027 (2001)
10. Forsythe, J., Hoffmann, K., Cummings, R., Squires, K.: Detached-eddy simulation with compressibility corrections applied to a supersonic axisymmetric base flow. J. Fluid Eng. **124**, 911–923 (2002)
11. Kawai, S., Fujii, K.: Computational study of a supersonic base flow using LES/RANS hybrid methodology. AIAA Paper 2004-68 (2004).
12. Fureby, C., Kupiainen, K.: Large-eddy simulation of supersonic axisymmetric baseflow. In: Turbulent Shear Flow Phenomena, TSFP3, Sendai (2003)
13. Sandberg, R., Fasel, H.: High-accuracy DNS of supersonic base flows and control of the near wake. In: Proceedings of the Users Group Conference, Nashville, pp. 96–104. IEEE Computer Society (2004)
14. Sandberg, R., Fasel, H.: Numerical investigation of transitional supersonic axisymmetric wakes. J. Fluid Mech. **563**, 1–41 (2006)
15. Sandberg, R.: Numerical investigation of turbulent supersonic axisymmetric wakes. J. Fluid Mech. **702**, 488–520 (2012)
16. Meliga, P., Sipp, D., Chomaz, J.: Elephant modes and low-frequency unsteadiness in a high Reynolds number, transonic afterbody wake. Phys. Fluids **21**, 054105 (2009)
17. Deck, S., Thorigny, P.: Unsteadiness of an axisymmetric separating-reattaching flow: numerical investigation. Phys. Fluids **19** (2007). doi:10.1063/1.2734996
18. Statnikov, V., Meiß, J.-H., Meinke, M., Schröder, W.: Investigation of the turbulent wake flow of generic launcher configurations via a zonal RANS/LES method. CEAS Space J. **5**, 75–86 (2013). doi:10.1007/s12567-013-0045-6
19. Saile, D., Gülhan, A., Henckels, A., Glatzer, C., Statnikov, V., Meinke, M.: Investigations on the turbulent wake of a generic space launcher geometry in the hypersonic flow regime. EUCASS Prog. Flight Phys. **5**, 209–234 (2013)

20. Statnikov, V., Glatzer, C., Meiß, J.-H., Meinke, M., Schröder, W.: Numerical investigation of the near wake of generic space launcher systems at transonic and supersonic flows. EUCASS Prog. Flight Phys. **5**, 191–208 (2013)
21. Saile, D., Gülhan, A., Henckels, A.: Investigations on the near-wake region of a generic space launcher geometry. AIAA 2011–2352 (2011)
22. Bitter, M., Scharnowski, S., Hain, R., Kähler, C.J.: High-repetition-rate PIV investigations on a generic rocket model in sub- and supersonic flows. Exp. Fluids **50**, 1019–1030 (2011)
23. Bitter, M., Hara, T., Hain, R., Yorita, D., Asai, K., Kähler, C.J.: Characterization of pressure dynamics in an axisymmetric separating/reattaching flow using fast-responding pressure-sensitive paint. Exp. Fluids **53**, 1737–1749 (2012)
24. Roidl, B., Meinke, M., Schröder, W.: A zonal RANS-LES method for compressible flows. Comput. Fluids **67**, 1–15 (2012)
25. Roidl, B., Meinke, M., Schröder, W.: Reformulated synthetic turbulence generation method for a zonal RANS-LES method and its application to zero-pressure gradient boundary layers. Int. J. Heat Fluid Flow **44**, 28–40 (2013).
26. Roidl, B., Meinke, M., and Schröder, W.: "Boundary layers affected by different pressure gradients investigated computationally by a zonal RANS-LES method," Int. J. Heat Fluid Flow **45**, 1–13 (2014).
27. Liou, M.S., Steffen, C.J.: A new flux splitting scheme. J. Comput. Phys. **107**, 23–39 (1993)
28. Boris, J., Grinstein, F., Oran, E., Kolbe, R.: New insights into large eddy simulation. Fluid Dyn. Res. **10**, 199–228 (1992)
29. Meinke, M., Schröder, W., Krause, E., Rister, T.: A comparison of second- and sixth-order methods for large-eddy simulations. Comput. Fluids **31**, 695–718 (2002)
30. Alkishriwi, N., Meinke, M., Schröder, W.: A large-eddy simulation method for low Mach number flows using preconditioning and multigrid. Comput. Fluids **35**, 1126–1136 (2006)
31. El-Askary, W., Schröder, W., Meinke, M.: LES of compressible wall-bounded flows. AIAA Paper 2003–3554 (2003)
32. Spalart, P., Allmaras, S.: A one-equation turbulence model for aerodynamic flows. AIAA Paper 92–0439 (1992)
33. Jarrin, N., Benhamadouche, N., Laurence, S., Prosser, D.: A synthetic-eddy-method for generating inflow conditions for large-eddy simulations. J. Heat Fluid Flow **27**, 585–593 (2006)
34. Pamiès, M., Weiss, P., Garnier, E., Deck, S., Sagaut, P.: Generation of synthetic turbulent inflow data for large eddy simulation of spatially evolving wall-bounded flows. Phys. Fluids **21**, 045103 (2009)
35. Schmid, P.J.: Dynamic mode decomposition of numerical and experimental data. J. Fluid Mech. **656**, 5–28 (2010)
36. Rowley, C.W., Mezic, I., Bagheri, S., Schlatter, P., Henningson, D.S.: Spectral analysis of nonlinear flows. J. Fluid Mech. **641**, 115–127 (2009)
37. Sayadi, T., Nichols, J.W., Schmid, P.J., Jovanovic, M.R.: Dynamic mode decomposition of h-type transition to turbulence. In: Proceedings of the Summer Program 2012, Center for Turbulence Research, Stanford, pp. 5–13 (2012)